ELSEVIER

Contents lists available at ScienceDirect

Chemical Engineering Science

journal homepage: www.elsevier.com/locate/ces



Chemical redox of lithium-ion solid electroactive material in a packed bed flow reactor



Devanshi Gupta a, Yuxuan Zhang b, Ziyang Nie a, Jing Wang a, Gary M. Koenig Jr a,*

- ^a Department of Chemical Engineering, University of Virginia, 102 Engineers' Way, P.O. Box 400741, Charlottesville, VA 22904, USA
- b Neutron Scattering Division, Oak Ridge National Laboratory, P.O. Box 2008, Oak Ridge, TN 37831, USA

HIGHLIGHTS

- Analysis of chemical redox between redox shuttles and solid particles.
- Framework for investigating lithium-ion electroactive material packed bed reactors.
- Demonstration reaction system of solid LiFePO₄ particles and soluble [Fe(CN)₆]³⁻.
- · Investigated impact of four variables on progression of chemical redox reaction.
- Packed bed system relevant to emerging flow battery and lithium recycling processes.

ARTICLE INFO

Article history: Received 29 July 2021 Received in revised form 21 December 2021 Accepted 15 January 2022 Available online 20 January 2022

Keywords: Chemical redox Lithium ion Packed bed reactor

ABSTRACT

Chemical redox reactions between solid electroactive materials and dissolved electroactive compounds are a necessary component of emerging technologies relevant to renewable energy including high energy density flow batteries and battery material recycling. In this work, an initial investigation of heterogeneous chemical redox for a packed bed reactor configuration between solid electroactive material and dissolved redox shuttles will be described. Experimental conditions including the height of the packed bed, the redox shuttle solution concentration, solution flow rate, and operating temperature were varied and their impact on the molar conversion of the solid electroactive material in the packed bed was quantified using electroanalytical techniques on the reactor effluent. The progression of the reaction and its dependence on the different variables explored will be discussed in the context of the limiting processes for porous packed aggregates of the solid electroactive material undergoing chemical oxidation.

© 2022 Elsevier Ltd. All rights reserved.

1. Introduction

With widespread deployment of renewable power sources such as solar and wind, large-scale energy storage will be needed to level these generation sources' intermittent loads (Gür, 2018). Among the electrochemical energy storage options available, redox flow batteries provide the advantage of separation of energy and power design and components, modularity, long cycle life, and versatility for stationary applications (Dunn et al., 2011). Conventional redox flow batteries use soluble electroactive species to store electrochemical energy. Hence, their volumetric energy density is limited by the solubility of these electroactive species, for example < 25 Wh L⁻¹ reported for systems such as all-vanadium (Wang et al., 2013). Recently, redox-targeting flow batteries (RTFBs) have been reported as a method to dramatically increase

Corresponding author.
 E-mail address: gary.koenig@virginia.edu (G.M. Koenig Jr).

the energy density of flow batteries (Yan and Wang, 2018; Vivo-Vilches et al., 2021; Páez et al., 2019; Wong and Sevov, 2021; Zanzola et al., 2017) In a RTFB system, the soluble electroactive species, referred to as redox shuttles, provide power in an electrochemical flow cell, as is the case for a conventional redox flow battery. However, unlike a conventional flow battery where the redox shuttles would also serve the role of storing all energy in the system, in a RTFB the vast majority of the energy is stored in solid electroactive species. Energy stored in the solid electroactive species is reversibly extracted via the redox shuttles by chemical reduction/oxidation reactions. The chemical redox of solid electroactive material is facilitated by contact with the soluble redox shuttles, provided the soluble shuttle is in the appropriate oxidation state and has sufficient potential driving force. The solid electroactive material is typically much more energy dense and is not limited by solubility in the electrolyte, and thus the incorporation of solid electroactive material can dramatically increase the volumetric energy density of the flow battery. Compared to redox flow

batteries based on only soluble electroactive materials, it has been estimated that RTFBs could have ten times the volumetric energy density (Jia et al., 2015). In contrast to alternative methods for high volumetric energy density flow batteries that take advantage of solid electroactive materials such as the use of suspensions or slurries (Duduta et al., 2011; Qi and Koenig, 2017), RTFBs have advantages of much lower viscosity in flowing through the electrochemical cell, while retaining the advantages of large surface area electrodes available for electrochemical reactions to occur and enable high current densities.

A RTFB overall system consists of coupled electrochemical and chemical reactors, as illustrated in Fig. 1a. There is a power stack where redox shuttles are electrochemically oxidized/reduced, and reservoirs where solid electroactive material is kept and undergoes chemical redox with the redox shuttles. At scaled operation, there will also be recirculation loops with pumps that transport redox shuttles between cell stacks and the chemical reservoirs, as well as additional components not shown such as power conditioning systems, controllers, etc. The design considerations of the electrochemical cell power stacks in RTFBs are similar to those of redox flow batteries and have been described previously (Chalamala et al., 2014). However, to the best of the authors' knowledge, the design principles for the chemical reservoir of the RTFB have not been well defined. Previous reports pertaining to the chemical reservoir have included characterization of the redox targeting process where the solid electroactive material was in the form of dispersed particles (Jia et al., 2015; Huang et al., 2013; Gupta and Koenig, 2020; Gupta et al., 2021), porous pellets (Vivo-Vilches et al., 2021), or electrode strips (Pan et al., 2014; Yan et al., 2018) have been reaction systems including batch reactors and continuous stirred tank reactors. These studies have provided fundamental insights to the chemical redox process and characterization of RTFB-type systems; however, it is not clear how well these model systems would translate at larger scales. While batch and stirred tank reactors with relatively low particle loadings are desirable for monitoring the chemical redox process, RTFB redox reactors will need to be flow-through to couple with the electrochemical cell, and low particle loadings reduce the volumetric energy density advantages of an RTFB system. Therefore, a packed bed reactor (PBR) comprised of a bed of the solid electroactive material particles could achieve both high volumetric chemical redox capacity and allow flow through of the electrolyte for coupling to the electrochemical flow cell (Cussler and Cussler, 2009).

In this study, a PBR has been evaluated where the solid electroactive material LiFePO4 (LFP) was oxidized by the redox shuttle [Fe(CN)₆]³⁻ (a photograph of the PBR can be found in Fig. 1b). As an initial investigation of a PBR for chemical redox relevant to a RTFB, the evaluation was focused on a single reaction (oxidation of LFP by the redox shuttle) in the PBR. It is noted that in a full system two reactions (oxidation and reduction of the solid electroactive material by redox shuttle(s)) will be needed for each chemical redox tank, and the tanks will need to be coupled to an electrochemical flow cell, LFP has advantages for use in a chemical redox PBR. LFP has a flat charge/discharge voltage at 3.45 V (vs. Li/Li+), and it has been well studied and commercialized for Li-ion battery applications and thus the detailed physical properties have been previously reported (Chung et al., 2002). During oxidation of LFP, Li* is removed from the structure and the Fe is oxidized from Fe2+ to Fe3+, resulting in FePO4 (FP). The flat charge/discharge voltage is desirable for a chemical redox PBR because the potential

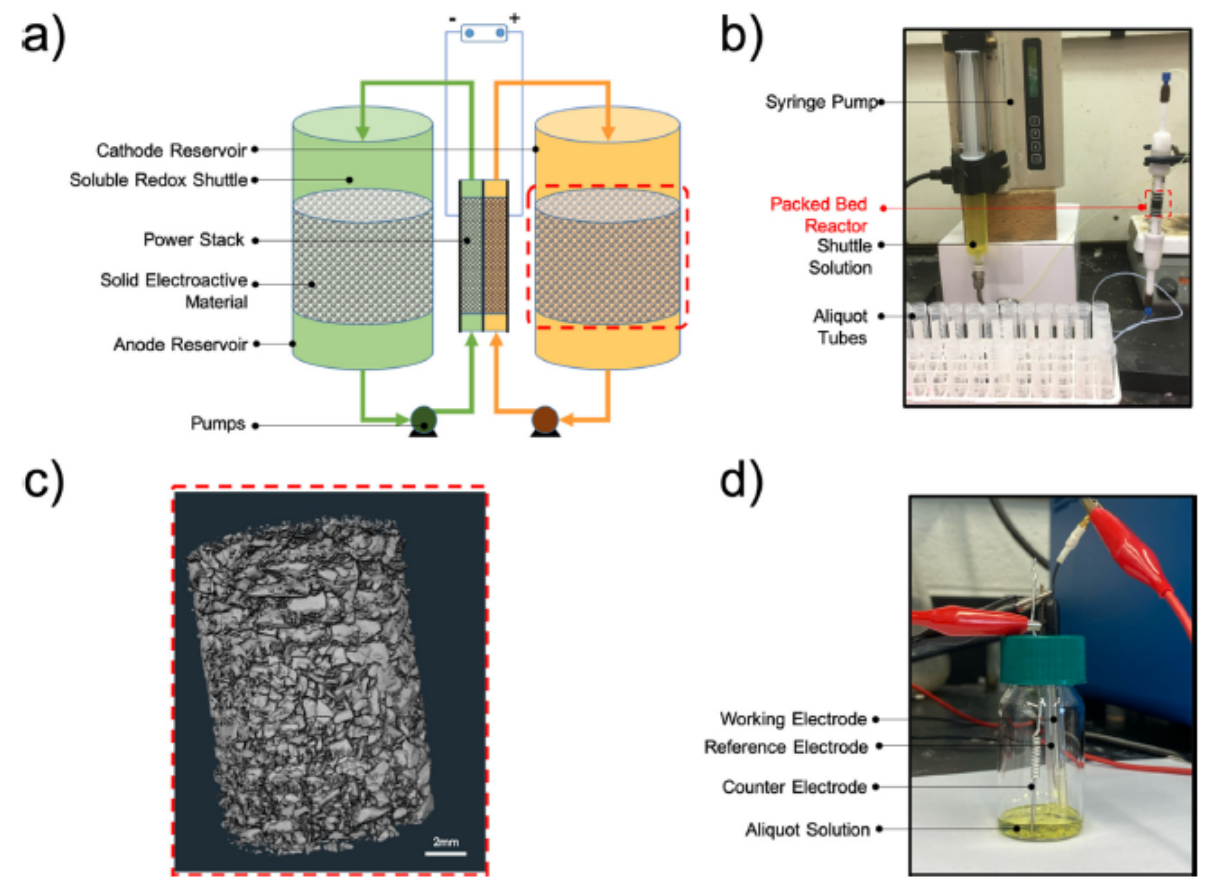


Fig. 1. a) Illustration of a full redox targeting flow battery system, with a red dashed box around the chemical redox reactor reservoir which this model study is directed towards. b) Photograph of the experimental setup for assessing the oxidation of LiFePO₄ with [Fe(CN)₆]³⁻. c) Three-dimensional reconstruction of a packed bed of LiFePO₄ as used in the experimental setup (the particle packed bed would be in the region with a red dashed box in b) from X-ray computed tomography. d) Photograph of the three-electrode setup used for electroanalytical analysis of aliquots collected from reactor effluent.

2

needed to oxidize or reduce the electroactive material does not shift as a function of the extent of lithiation of the solid electroactive material. The reaction between LFP and $[Fe(CN)_6]^{3-}$ is expected to proceed as shown below:

$$LiFePO_4 + [Fe(CN)_6]^{3-} \rightarrow FePO_4 + [Fe(CN)_6]^{4-} + Li^+$$
(1)

In this manuscript, the influence of four variables on the measured conversion of [Fe(CN)₆]³⁻ to [Fe(CN)₆]⁴⁻ in the effluent of a PBR loaded with LFP (which was correspondingly converted to FP) will be investigated. The LFP - [Fe(CN)₆]³⁻ redox system was recently reported to have fast kinetics (Yu et al., 2019) and excellent first-cycle reversibility of 99% (Vivo-Vilches et al., 2021), making it a robust choice for assessing the design of the chemical reservoir of an RTFB. The four variables evaluated were: height of the LFP packed bed, concentration of [Fe(CN)₆]³⁻ in the electrolyte, flow-rate of electrolyte containing $[Fe(CN)_6]^3$ -,and the temperature of the reactor and solution fed. Three to four variations were conducted for each variable evaluated. Single variable analysis of variance (ANOVA) was used to assess whether there were measurable changes in the conversion of the LFP in the PBR. This study provides insights useful to designing chemical redox-based systems and a framework for evaluating redox shuttles and solid electroactive material pairings. While the chemical redox has been motivated by RTFBs, such experiments can provide insights relevant to other applications/systems relying on chemical redox as well, such as photochemical flow batteries (Li et al., 2015; Liao et al., 2016), overcharge protection of Li-ion batteries (Zhang et al., 2012; Moshurchak et al., 2005), and battery recycling (Yu et al., 2019).

2. Materials and methods

2.1. Materials

Commercial carbon coated LFP (Xiamen TOB New Energy Technology, China), potassium ferricyanide ($K_3[Fe(CN)_6]$, Sigma Aldrich), potassium ferrocyanide ($K_4[Fe(CN)_6]$, Sigma Aldrich), and lithium sulfate (Li_2SO_4 , Fisher Scientific) were used as received without further purification.

2.2. Methods

2.2.1. Mildly sintered LFP pellet preparation

Directly packing the column with the fine LFP powder resulted in low flow rates of the fluid through the column, thus the LFP was mildly sintered to prepare coarser aggregates. To prepare the sintered LFP pellet, 1.5 g LFP active material powder was loaded into a 16 mm diameter Carver pellet die and pressed with 12,000 lb_r for 2 min in a Carver hydraulic press. Next, the pellets were heated in a Lindberg/Blue M tube furnace from room temperature to 400 °C at a ramp rate of 1 °C min $^{-1}$ under N_2 atmosphere, with an inert atmosphere chosen to minimize the possibility of oxidation of the LFP. After holding at 400 °C for 1 h, the furnace was cooled to room temperature at a rate of 1 °C min $^{-1}$. The diameter of the sintered pellets was $\sim\!16$ mm and thicknesses were approximately 2.5 mm.

2.2.2. Powder X-ray diffraction

The structure of the active material that comprised the sintered pellets was confirmed to contain the same bulk material structure as the as-received LFP material using X-ray diffraction (XRD). XRD was collected using Panalytical X'pert diffractometer with Cu K α radiation between 2 θ values of 15 and 40 $^{\circ}$.

2.2.3. Packed bed reactor

Sintered LFP pellets were coarsely pulverized using a mortar and pestle by hand. After that, the sintered LFP powder was weighed and then loosely packed into a glass chromatography column (Cole Parmer, 10 mm diameter, adjustable height). Teflon frits (Cole Parmer, 5 μ m) were used on either end of the packed bed to constrain sintered LFP powder inside the column. The flow rate of [Fe(CN)₆]³⁻ solution prepared by dissolving K₃[Fe(CN)₆] in deionized (DI) water was regulated using a syringe pump (KDS 100 series). A picture of the PBR experimental setup can be found in Fig. 1b.

The experimental conditions used in this study are listed in Table 1. Further discussion of the selection of the experimental conditions can be found in the Supplementary Material. The bed height was varied from 0.5 to 1.5 cm with corresponding loading of 0.5–1.5 g sintered LFP resulting in the total combined pore/void volume fraction being constant at approximately 0.63. To study the effects of varying $[Fe(CN)_6]^3$ — concentration on LFP conversion, $[Fe(CN)_6]^3$ — concentrations of 0.1, 0.2, and 0.3 mol L⁻¹ were evaluated . For estimating the LFP conversion dependence upon flow rate of $[Fe(CN)_6]^3$ — solution, flow rates of 30, 42, 54 and, 66 mL h⁻¹ were used. Except for the experiments where concentration was varied, a $[Fe(CN)_6]^3$ — concentration of 0.2 mol L⁻¹ was used. Except for experiments where bed height was varied, a bed height of 1 cm was used. Except for experiments where temperature was varied, the reaction was conducted at room temperature, measured to be 22.4 °C

The effects of temperature on conversion in the PBR were conducted at 4.0, 13.0, 22.4, and 40.0 °C. The 22.4 °C case was room temperature. For the other 3 cases, a water bath (Lauda Brinkmann RC-20) was used to maintain both the packed bed and the [Fe $(CN)_6$]³⁻ feed solution at 4.0, 13.0, or 40.0 °C. The feed solution and LFP packed bed setup were equilibrated at 4.0, 13.0, or 40.0 °C for 1 h in the water bath before running the reaction. The water bath temperature was observed to always stay within ±0.2 °C of the set point. The measured temperature of the feed solution in the syringe was typically offset by -0.5 °C relative to the water bath set point.

Before starting to feed the $[Fe(CN)_6]^{3-}$ solution, the packed LFP bed was rinsed using DI water at the same flow rate as used during the reaction. Thus, there was an initial volume of water that exited the reactor which was accounted for in conversion determinations. After each experiment, the packed LFP bed was purged with 60 mL DI water at 40 mL h⁻¹ to remove any remaining $[Fe(CN)_6]^{3-}$. The remaining powder (usually a blend of unreacted LFP and LFP converted to FP) was then dried overnight in a fume hood, and subsequently dried an additional 8 h in an ambient oven at 80 °C, followed by an additional 4 h of drying in a vacuum oven at 80 °C. In some cases, the dried LFP/FP after reaction of the LFP with $[Fe(CN)_6]^{3-}$ was used for further electrochemical and materials characterization.

2.2.4. Cyclic voltammetry

Under every experimental condition described in the previous section, the effluent from the reactor was continuously collected in 2 mL increments. Each 2 mL aliquot was analyzed using cyclic voltammetry (CV) sweeps in a three-electrode system: Pt microelectrode (100- μ m diameter, BASi) as the working electrode, Pt wire (1 mm diameter, 4 cm length, Sigma Aldrich) as the counter electrode, and Ag/AgCl (immersed in KCl gel electrolyte, 74 mm length Ag wire, Pine research) as the reference electrode. A picture of the three-electrode system can be found in Fig. 1d. The feed solution of $[Fe(CN)_6]^{3-}$ was analyzed at 20, 40, 60, 80, and 100 mV s^{-1} from 0.0 to 0.5 V (vs. Ag/AgCl) before each experiment to assess that the effective diffusion coefficient of the redox shuttle and the measured currents were consistent. The diffusion

Table 1
Experimental conditions used in this study.

Temperature (°C)	LFP bed-height (cm)	Flow rate (mL hr ⁻¹)	Shuttle concentration (mol L ⁻¹)	Shuttle volume (mL)
22.4	0,5	30	0.2	30
22.4	1.0	30	0.2	60
22.4	1.5	30	0.2	90
22,4	1.0	42	0,2	60
22,4	1.0	54	0.2	60
22.4	1.0	66	0.2	60
22.4	1.0	54	0.1	60
22.4	1.0	54	0.3	60
4.0	1.0	54	0.2	60
13,0	1.0	54	0,2	60
40.0	1.0	54	0.2	60

coefficient of $[Fe(CN)_6]^{3-}$ estimated using Randles-Sevcik Equation was found to be $2.49 \pm 1.15 \times 10^{-6}$ cm² s⁻¹, in agreement with previous reports (Baur and Wightman, 1991). For each aliquot of the reactor effluent, CV sweeps were conducted at 20 mV s⁻¹ between 0.0 and 0.5 V (vs. Ag/AgCl) and using the diffusion coefficient estimated from the previous step and the Randles-Sevcik equation, the concentration of the $[Fe(CN)_6]^{3-}$ species was determined. In general, the $[Fe(CN)_6]^{3-}$ in the effluent was lower than the $[Fe(CN)_6]^{3-}$ in the feed due to conversion to $[Fe(CN)_6]^{4-}$, and reduction of each mol of $[Fe(CN)_6]^{3-}$ was assumed to correspond to the oxidation of one mol of LFP to FP. The measured peak current from the CV scans was confirmed to have a linear dependence on the relative fraction of $[Fe(CN)_6]^{3-}$ in solution (see Supplementary Material for additional details and CV results in Figure S1).

CV scans were also conducted on the LFP solid electroactive material. For electrochemical evaluation, the LFP powder was processed into an electrode. LFP electrodes were made by mixing a slurry of LFP, carbon black, and polyvinylidene fluoride (PVDF, Sigma Aldrich) in 8:1:1 ratio by mass using N-methyl-2pyrrolidone (NMP, Sigma Aldrich) as solvent. The slurry was then coated on rectangular strips of Ni foam (1 cm x 5 cm) and dried overnight at 80 °C in an oven. Electrodes were then evaluated in a three-electrode system: LFP coated within Ni foam as the working electrode, Pt wire as the counter electrode, and Ag/AgCl (in concentrated KCl gel) as the reference electrode. The electrolyte was 0.1 mol L-1 Li2SO4 dissolved in DI water. CV scans of the LFP electrode were collected at 0.02 mV s^{-1} between -0.1 - 0.5 V vs. Ag/ AgCl (example scans can be found in Supplementary Material, Figure S2a). The half-wave potential of LFP determined from the scans was 0.186 V (vs. Ag/AgCl), which translated to 3.425 V vs Li/Li* and was consistent with previous reports (Padhi et al., 1997; Yuan et al., 2011).

The CV scans for 0.1 mol L^{-1} [Fe(CN)₆]³⁻ solution in the electrolyte used for the LFP CV experiments (0.1 mol L^{-1} Li₂SO₄ aqueous solution) can be found in Supplementary Material, Figure S2b. The estimated half-wave potential of [Fe(CN)₆]³⁻ was 0.247 V (vs. Ag/AgCl), consistent with previous literature (Luo et al., 2017).

2.2.5. X-ray computed tomography

The column samples for X-ray computed tomography (XCT) were made using Teflon cylinders, and mimicked the PFR column shown in Fig. 1b (details in Supplementary Material, Figure S3). XCT was performed on a Zeiss Xradia Versa 520 at Oak Ridge National Laboratory. The X-ray source was tuned to 80 kV and operated at 6 W to achieve ~20% transmission. And 0.4x optics was chosen on the detector side to fill the detector field of view (FOV) with the full Teflon cylinder. Under this configuration, the effective pixel size was about 16 μm. For the XCT acquisition, 1601 evenly spaced projections, each with 4 s exposure, were collected over 360° rotation. These collected projections were then loaded into Zeiss reconstruction tool, which completes the

filtered-back-projection (FBP) based reconstruction. Image processing and analysis were performed using Amira Avizo software. The XCT setup is detailed in the Supplementary Material and a 3-D reconstruction of LFP packed bed is shown in Fig. 1c.

2.2.6. Coin cell fabrication and electrochemical characterization

The electrochemical properties of as-received LFP, sintered LFP, and the oxidized LFP (FP) after reaction with [Fe(CN)₆]3- was evaluated using 2032-type coin cells on a MACCOR battery cycler. The FP after oxidation by [Fe(CN)₆]3- was harvested from the column after the following reaction conditions: 0.3 mol L-1 [Fe(CN)6]3was flowed at 54 mL hr⁻¹ for 67 min through a 1.0 cm LFP packed bed height (containing 1.0 g LFP powder). Based on CV scans on the PBR effluent aliquots, the conversion of the LFP was estimated to be 100%. Using the electroactive materials, cathodes were fabricated consisting of a slurry of 80:10:10 (by wt%) active material: carbon black: PVDF, where the active material was LFP, sintered LFP, or FP after oxidation by [Fe(CN)6]3- (which was the sintered LFP after the chemical oxidation process). The components were blended into a slurry with NMP as solvent. Prior to adding NMP, the active material and carbon black were blended together using a mortar and pestle. Hence, the materials with aggregation due to the mild sintering process (LFP after sintering, and the material after sintering and then oxidation to FP using K3[Fe(CN)6]) likely had some reduction in aggregate size due to pulverization with the mortar and pestle. The slurry was cast on an aluminum current collector using a doctor blade with a gap height of 125 µm. The electrodes were then dried overnight in an ambient oven at 80 °C, and then in a vacuum oven for two hours at 80 °C. The thickness of the electrodes, measured using a digital micrometer, was found to be 100 ± 5 μm for LFP, 70 ± 3 μm for sintered LFP, and 70 ± 3 μm for FP from oxidation of sintered LFP with $[Fe(CN)_6]^{3-}$. The active material loading was 9.7 ± 0.2 mg cm⁻² for LFP, 9.4 ± 0.2 mg cm⁻² for sintered LFP and, 9.1 ±0.1 mg cm⁻² for FP from oxidation of sintered LFP with $[Fe(CN)_6]^{3-}$. The errors were the standard deviation of three independent measurements of thickness and loading on separate electrode regions or punched samples, respectively. Punched Li foil discs (1.6 cm² area, 100 µm thickness) were used as the anode, 1.2 mol L-1 LiPF6 in 3:7 vol% ethylene carbonate:ethyl methyl carbonate (Gotion Inc.) was used as the electrolyte, and electrodes were separated using glass fiber separators (Fischer Scientific, G6 0.32 mm thickness). Three cells were made for each cathode active material. The cells were charged at room temperature with the same charge and discharge rate at C/20, C/10, C/5, C/2, 1 C and, C/20, where 1C was assumed to correspond to 160 mAh g⁻¹ active material in the electrode, based on the voltage profiles obtained at C/20 rates for each material (Supplementary Material, Figure S4a). The first two charge/discharge cycles for sintered LFP and LFP after reaction in the PBR can be found in Supplementary Material, Figures S4b,c. Note that after oxidation of LFP in the PBR to FP the first cycle was a discharge to reduce/lithiate the

FP back to LFP. As nearly the same gravimetric capacity for LFP was obtained during the first discharge of the FP material, this result was consistent with complete oxidation/conversion of the LFP material the PBR. For rate capability experiments, three cycles at each C rate were performed, totaling 18 cycles. Representative charge/discharge capacities for the cycling of the cells at different C rates can be found in the Supplementary Material, Figure S5. Note that the Li/LFP and Li/sintered LFP cells were started with a charge cycle and Li/FP (where FP was LFP after chemical oxidation by K₃Fe(CN)₆) cells were started with a discharge cycle. The voltage window for all electrochemical measurements was 2.5 to 4 V (vs. Li/Li*)

2.2.7. Material characterization and analysis

The morphologies of original LFP, sintered LFP (after breaking into aggregates using mortar and pestle by hand), and FP (oxidized with [Fe(CN)₆]³⁻) were observed using scanning electron microscopy (SEM, Quanta 650 SEM). X-ray diffraction patterns were taken of these three materials along with FP prepared via chemical oxidation with an alternative previous reported method as a reference (Lepage et al., 2014). The surface area of the original and sintered LFP, as determined using the Brunauer-Emmett-Teller (BET) method, was measured using a Micromeritics ASAP 2020 at 77 K using nitrogen as the adsorbing gas. Pore sizes from the nitrogen adsorption isotherms were calculated using the Barrett-Joyner-Halenda (BJH) method.

3. Results and discussion

LFP is a popular electroactive material used in the cathode of Liion batteries, containing earth-abundant Fe as the transition metal and demonstrated to have favorable cycle life and safety outcomes (Padhi et al., 1997; Zubi et al., 2018). These features make LFP an attractive option for RTFBs designed for grid-scale storage, as resource abundance/low cost and long-term reliability/cycling are key qualities for the stationary energy storage applications likely best suited to RTFBs (Yan and Wang, 2018). LFP also has a flat half-wave potential at 3.45 V (vs. Li/Li+) which offers advantages for RTFBs. First, a flat potential means that the overpotential needed from the redox shuttle to drive LFP oxidation or FP reduction would be expected to be relatively constant across a wide range of states of charge. Second, the half-wave potential of LFP is well within the stability window of both aqueous and nonaqueous electrolytes, hence allowing a significant range of oxidizing redox shuttles and electrolytes that would be compatible with LFP.

[Fe(CN)₆]3- and its reduced form, [Fe(CN)₆]4- are stable and reversible redox shuttles that have been demonstrated in aqueous flow batteries with excellent cyclability (Luo et al., 2017; Gong et al., 2015; Luo et al., 2019). Recently, rapid kinetics were demonstrated for chemical oxidation of LFP with $[Fe(CN)_6]^{3-}$ in a threeelectrode cell, where 95% of [Fe(CN)6]3- was reduced by 3 times equivalent capacity of LFP (Yu et al., 2019). Hence, this promising reported result motivated the selection of the LFP and [Fe (CN)₆|3- chemical redox reaction for this initial demonstration of a chemical redox PBR (Vivo-Vilches et al., 2021; Chen et al., 2019). CV scans on [Fe(CN)₆]³⁻/[Fe(CN)₆]⁴⁻ solutions resulted in a measured half-wave potential of 0.247 V (vs. Ag/ AgCl), which was 60 mV higher than LFP (relevant CV scans can be found in Supplementary Material, Figure S2). As the relative fraction of [Fe (CN)6]3- in prepared solutions with different concentrations of [Fe(CN)₆]³⁻/[Fe(CN)₆]⁴⁻ was varied, relatively small variations in half-wave potential were observed (from 0.248 V to 0.220 V vs. Ag/AgCl, as shown in Supplementary Material, Figure S1). Therefore, a driving potential of 30-60 mV was assumed between LFP and [Fe(CN)₆]³⁻ to favor reaction (1) proceeding throughout the PBR, until the LFP was nearly completely converted to FP.

Since chemical redox between solid electroactive materials and redox shuttles occurs on the surface of solid particles, the rate of the chemical redox can be increased by selecting smaller solid electroactive materials with higher surface area. However, with high surface area solid electroactive material, a PBR configuration results in high pressure drop and therefore high parasitic loss in pumping the electrolyte solution (Cussler and Cussler, 2009). Even in the experimental system herein, directly packing the as received LFP material in the column significantly reduced the achievable flow rates. In addition, it was desired to minimize the possibility of the particles leaving the reactor. In a full RTFB, free particles would start to aggregate at the porous electrodes in the electrochemical power stack, resulting in increased pressure drop and parasitic pumping losses. For the experimental analysis in this study, free particles could potentially continue chemical redox within the collected aliquots, which would have resulted in higher observed chemical redox reactions across the column than actually achieved. Thus, to mitigate these issues, the as-received LFP powder was mildly thermally treated in a flowing N2 atmosphere to provide coarser LFP aggregates - although it is noted the aggregates were still expected to contain internal porosity in the PBR.

These design considerations were navigated by sintering fine LFP powder (\sim 60 nm average particle lengths) into pellets. Those pellets were then coarsely pulverized to secondary particle sizes ranging from 16 μ m to several mm, as can be seen in the XCT image in Fig. 2c and 2d.

3.1. LFP/FP characterization as-received, after sintering, and after chemical oxidation

The sintering of LFP powder was performed to mitigate the extreme pressure drop originating from a packed bed composed of fine particles. However, it was desired to retain the primary particle size of the LFP to maintain high total surface area available for chemical redox reactions and to mitigate transport of Li* and ewithin the primary particles drastically reducing the achievable reaction rate (Gaberscek et al., 2007). Mild sintering at 400 °C has been shown to be sufficient to form particle connections but still retain electrochemical activity for LFP (Ravet et al., 2007). SEM images confirmed the primary particle size did not dramatically increase after sintering of LFP particles at 400 °C (Fig. 3a,b). Secondary particle aggregates were difficult to assess; however, secondary aggregates tens of micrometers were observed in SEM (examples can be found in Supplementary Material, Figure S6). Furthermore, the XRD patterns revealed peaks consistent with LFP both before and after the mild sintering step, and no impurity peaks were observed in either pattern (Fig. 4a). Electrochemical analysis of coin cells with LFP active material both before and after the sintering process demonstrated that the capacity at cycling rates between C/20 and C/5 were nearly identical, suggesting that electrochemically active LFP was retained after the sintering and hand grinding process (see Supplementary Material, Figure S5). It is noted that the capacity at the two highest rates was significantly lower for the sintered LFP, although the capacity at low rates conducted after the high rate cycling was recovered, suggesting the decreased capacity was not due to irreversible capacity loss. The lower capacity at high rates may have been due to different transport properties in the electrode microstructure for the larger aggregates, though exploration of the root cause of the high rate capacity difference was not pursued and this speculation was not experimentally verified.

The sintered LFP was used in the PBR experiments. To confirm the material was still an electroactive powder after chemical oxidation, the powder was harvested after being oxidized in the PBR

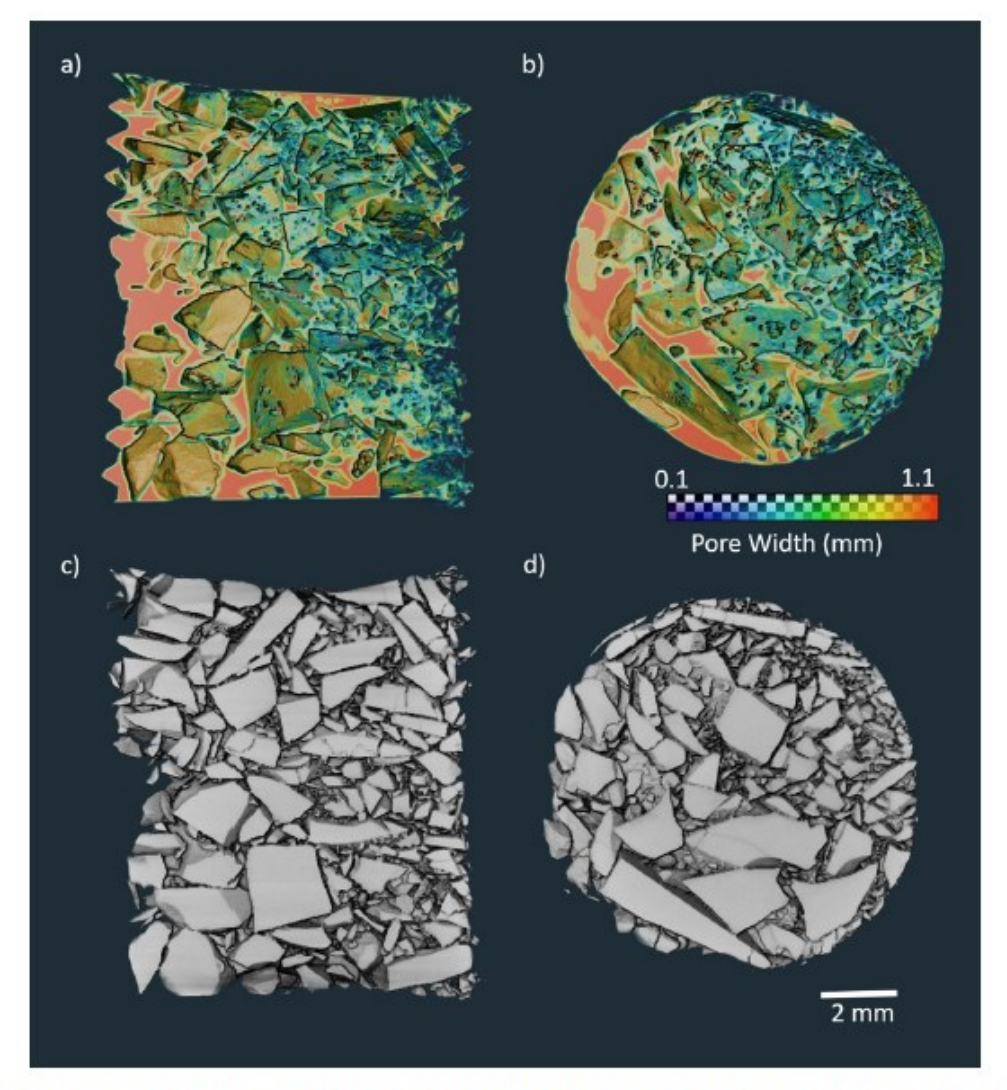


Fig. 2. XCT reconstructions of the packed bed reactor. Two-dimensional slices of the pore volumes are shown for a) the vertical length of the column and b) the horizontal radial axis at the center of the column. The color scale corresponds to the relative longest lengths of a given pore/void. Two-dimensional slices of the LFP aggregates are shown for c) the vertical length of the column and d) the horizontal radial axis at the center of the column. Note that XCT resolution was not sufficient to show internal porosity in the LFP aggregates.

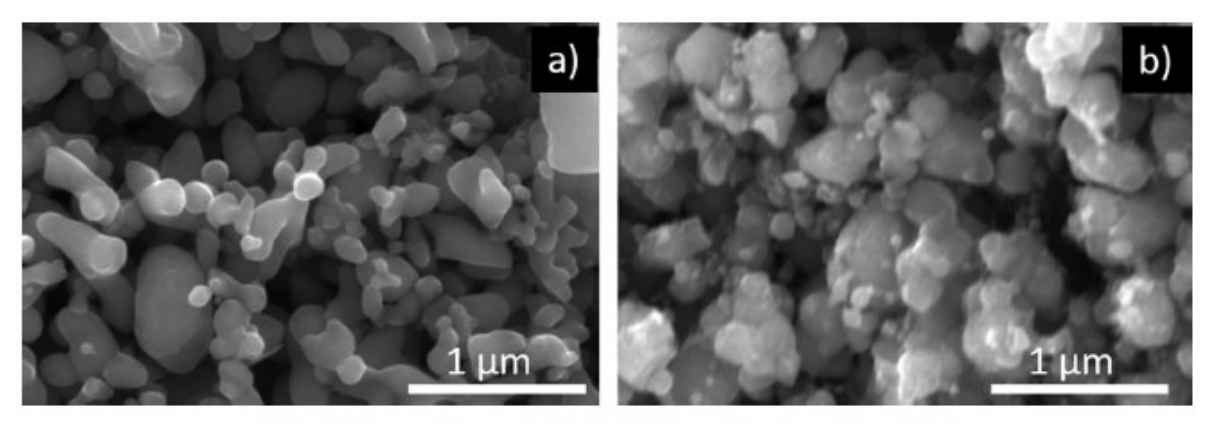
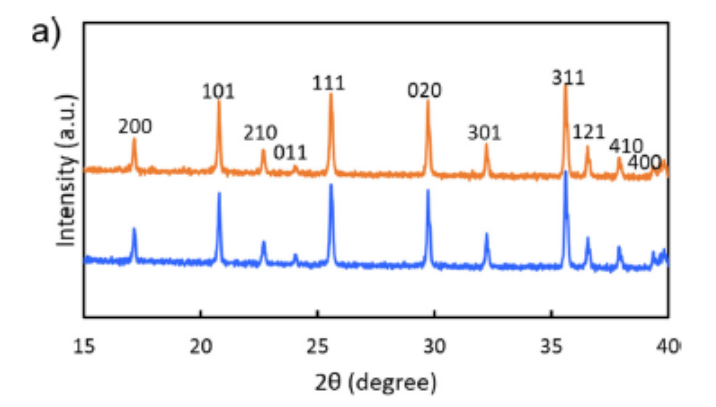


Fig. 3. SEM images of a) as-received LFP and b) sintered LFP after grinding by hand.

and then characterized. The LFP was chemically oxidized using 0.3 mol L⁻¹ [Fe(CN)₆]³⁻, and via analysis of the effluent the conversion of the LFP to FP was estimated as 100%. This powder of LFP oxidized to FP was evaluated using XRD (Fig. 4b), and the patterns were in agreement with a previously established method for chemically oxidizing LFP to FP with H₂O₂ (Lepage et al., 2014). Coin cells

made using LFP chemically oxidized to FP from the PBR had a reversible electrochemical capacity at C/20 comparable to the as-received material (for charge and discharge capacity from rate capability testing, see Supplementary Material, Figure S5). SEM images of the material collected after oxidation and 100% conversion to FP in the PBR can be found in Supplementary Material,



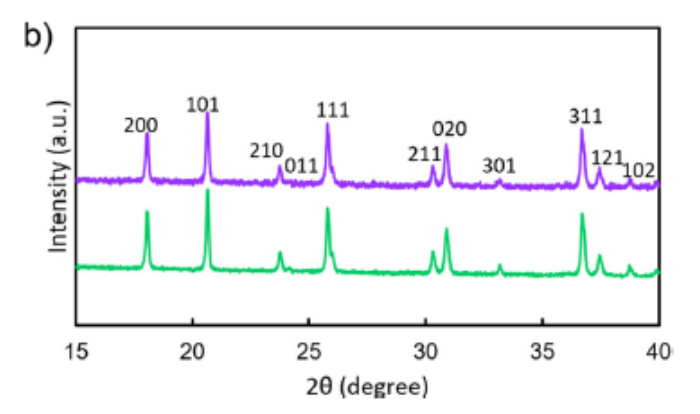


Fig. 4. a) XRD patterns of as-received LFP (blue) and sintered LFP (orange). b) XRD patterns of FP obtained after oxidation of the LFP to FP using hydrogen peroxide via a procedure previously reported (green) (Kuss et al., 2014), and LFP after reaction with [Fe(CN)₆]³ (purple), where analysis of reactor effluent indicated full conversion of the LFP to FP. Patterns were consistent with PDF- 01-078-7908 for LFP in a) and PDF- 04-017-0610 for FP in b).

Figure S7. The SEM results suggested the primary particle morphology was retained after the reaction in the PBR.

3.2. Pore structure and XCT analysis

The BET surface area of sintered particles was 8.8 m² g⁻¹ compared to 11.3 m² g⁻¹ for the original LFP powder. This reduction of surface area may have in part been due to increased primary particle size, but even though the heat treatment was in inert atmosphere there was likely some oxidation of the carbon coating which may have significantly contributed to the surface area reduction. The pore width distribution was calculated using the BJH method, and can be found in Supplementary Material, Figure S8).

The particle and pore/void distribution in the PBR were also analyzed using the XCT images. Fig. 2a,b are the distance maps of the pores along the length and radial direction, respectively, in the LFP PBR. XCT pixel pitch was 15.9 µm, so only relatively large-scale pores and particles can be analyzed, and internal porosity of the LFP aggregates was not accessible. The pore area distribution is shown in Supplementary Material, Figure S9. On a number basis many of the pores were near the limit of what can be detected in XCT, and thus the extent to which some of the smallest pores from XCT were artifacts was less clear. In any case, the analysis suggested there were many pores with areas < 0.1 mm² both on a number and total volume basis, and on a volume basis there was also a significant number of pores between 0.2 and 0.4 mm² area, Fig. 2c,d show the 3D reconstruction of LFP particles. The particle size distribution was extracted from this XCT image and the outcomes can be found in Supplementary Material, Figure S10,

On a number basis, most particles detected in XCT were only a few pixels in size, where it would be difficult to resolve the detailed distribution. However, on a volume basis, over 99.7% of the particle volume was particles with lengths over 0.5 mm. As the total moles of LFP available is dependent on particle volume, >99.7% of the LFP available to react was in particle aggregates > 0.5 mm as determined by XCT analysis.

Based upon the mass of LFP added in the column analyzed with XCT and the crystal density of LFP, volume fraction of pores/voids should have been 0.634. The total pore void fraction was 0.138 from the XCT analyzed region. This would suggest that ~41% of the particle aggregates were voids/pores to match the geometric porosity for the column based on the particle loading. Thus, the XCT analysis suggested the LFP moles available to react was primarily in large aggregates with approximately 41% porosity which would be filled with electrolyte, although there were likely smaller particles between the large aggregates that contributed a relatively small amount to the chemical redox reaction but may have interacted with the electrolyte fluid flowing past to for example provide additional drag.

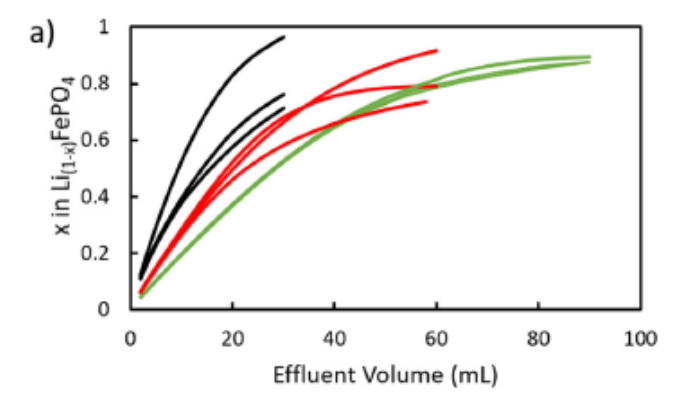
3.3. Reactor parameters investigated

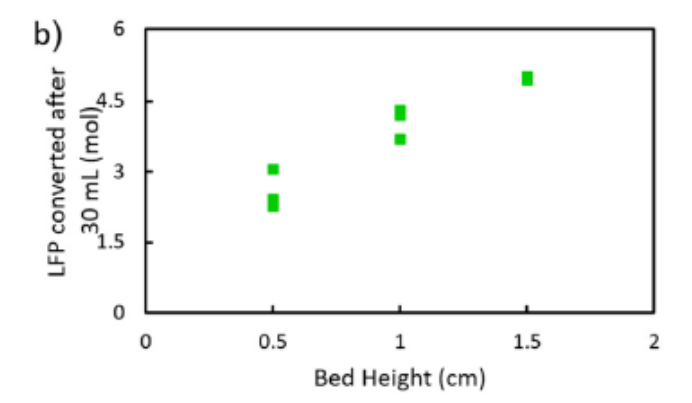
Four parameters were independently adjusted to evaluate their influence on the conversion in the PBR as a function of time during chemical oxidation of LFP with [Fe(CN)6]3-: 1) height of the bed packed with solid electroactive material, 2) flow-rate of the feed containing redox shuttle, 3) redox shuttle ([Fe(CN)₆]³⁻) concentration, and 4) temperature of the chemical reservoir and the feed solution (with both matched to the same temperature). Bed height and concentration of redox shuttle are design variables and can be built into the design of the PBR prior to operation. Flow rate of redox shuttle containing electrolyte was an operational variable and can be varied during the operation of the PBR, although for a given experimental run the flow rate was maintained at a single value. Temperature could in principal be actively adjusted within the PBR, though for the experiments herein it was maintained at a single value through immersion of the PBR and feed solution reservoir in a temperature-controlled bath, All experimental test conditions are listed in Table 1. Outcomes were assessed using single-factor ANOVA (Navidi, 2008). In this study, conversion of LFP in the packed bed was the dependent variable, and bed height, flow rate, [Fe(CN)₆]³ - concentration, and reactor temperature were the independent variables. The null hypothesis was that observed variation in conversion for a sample set was due to the random variation in the measured conversions. Rejection of the null results in acceptance of the alternative hypothesis, which in this study was the conclusion that conversion of LFP was influenced by changes in the variable of interest. The p-value, that measures the plausibility of the null hypothesis, was used at the threshold of 5%. If p-value was less than 0.05, the null hypothesis was rejected, and the alternative hypothesis was accepted. However, if the p-value was greater than 0.05, then the null was not rejected. In that case, both null and alternative hypothesis were plausible.

3.3.1. Bed-height

Keeping the mass of LFP powder per bed volume and flow-rate constant, the bed height of the PBR was varied at 0.5, 1.0, and 1.5 cm containing 0.5, 1.0, and 1.5 g LFP, respectively. The temperature for all experiments was room temperature, measured to be 22.4 °C. The feed solution for all experiments contained 0.2 mol L^{-1} [Fe(CN)₆]³⁻, and the feed solution flow rate was 30 mL hr⁻¹. The duration of time that the feed solution was fed through the PBR was chosen such that the volume of electrolyte flowed through each bed height contained a total of ~ 2 times moles of redox shuttle relative to the moles of LFP in the packed bed reactor. In other

words, the total [Fe(CN)6]3- fed through the PBR for each experiment was chosen to result in ~ 2 times the stoichiometric moles required to fully oxidize the LFP powder in the PBR. The results of varying bed height are shown in Fig. 5a-c. Experimental conditions were run in triplicate with each line in Fig. 5a,c representing a separate experiment, and each data point in Fig. 5b corresponding to an experiment, Fig. 5b contains just the total moles of LFP converted after 30 mL of redox shuttle solution had passed through the column, with each data point representing a different experiment. This analysis is shown because the stoichiometry in Fig. 5a corresponds to different total moles of LFP because the greater height has more total moles of LFP loaded in the column. It is noted that the two shorter bed heights in Fig. 5a (0.5 and 1.0 cm) had much more variation in the conversion as a function of effluent volume/reaction time. It is speculated this may have been due to variations in bed packing, where for example the packing could





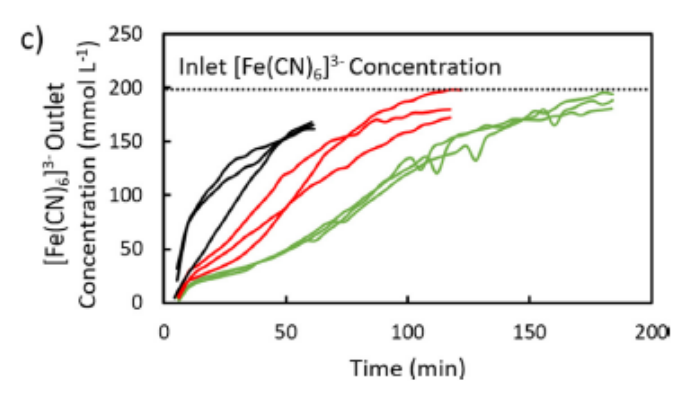


Fig. 5. a) Conversion of LFP solid material in the reactor at different bed heights of 0.5 cm (black), 1.0 cm (red), and 1.5 cm (green) as a function of volume of redox shuttle solution fed. b) Total moles of LFP converted (FP generated) as a function of bed height for the same 30 mL volume of 0.2 mol L⁻¹ [Fe(CN)₆]³⁻ flowed through the column. c) Outlet [Fe(CN)₆]³⁻ concentration as a function of time. Experimental conditions were run in triplicate, and each experiment is a different line in a) and c), and data point in b).

result in zones where the fluid bypasses some of the particle regions and those regions/particles do not react as completely. Such an effect would be expected to result in greater variability in LFP conversion for columns with lower total thickness/volume, where a relatively small bypassed zone would have a proportionally greater impact on the total measured conversion of LFP in the column.

The molar conversion of LFP to FP after completing flowing 2 mol [Fe(CN)6]3- per mol of LFP for the different bed heights varied between 81 and 88%, with the 1.5 cm bed height having a slightly higher conversion (Supplementary Material, Table S1). However, there was not a significant difference of conversion between the three bed heights after flowing through equivalent molar stoichiometries of [Fe(CN)6]3-, as determined by one-way ANOVA (p = 0.624). Hence, when proportional total moles of [Fe(CN)₆]³⁻ solution was flowed through different packed bed heights, similar molar conversion of LFP was achieved. However, when LFP conversion was measured for the same amount of [Fe(CN)₆]³ solution (30 mL, 6 mol) flowed through, there was a significant difference between molar conversion of LFP in different bed heights (p = 0.00024). Thus, if same amount of $[Fe(CN)_6]^{3-}$ was flowed then the molar conversion of LFP had a linear correlation to bed height, as shown in Fig. 5b. Therefore, molar conversion of LFP was dependent upon bed-height for the same moles of redox shuttle flowed through, but for the same molar ratio of LFP to redox shuttle there was not a significant difference in conversion.

3.3.2. Flow rate variation

For constant bed height (1.0 cm) and concentration (0.2 M [Fe (CN)₆]³⁻), four flow rates were evaluated at room temperature: 30, 42, 54, and 66 mL h⁻¹ corresponding to average residence times of 94, 67, 52, and 43 s, respectively. The molar ratio of total moles [Fe(CN)₆]3- fed to the column to LFP in the packed bed was again two for the conditions tested. The Reynolds number for the range of flow rates was estimated as 1.0 \times 10⁻² to 2.2 \times 10⁻² (Rawlings and Ekerdt, 2002), hence the flow through the column was expected to occur in the laminar regime. As shown in Fig. 6, the molar conversion of LFP for 30 and 54 mL hr^{-1} was \sim 82%, whereas it was 73% and 77% for 42 and 66 mL h-1, respectively, after flowing all the electrolyte through the PBR. Therefore, flowrate of [Fe(CN)6]3- solution did not have a significant effect on the molar conversion of the LFP packed bed for the range of flow rates tested (p = 0.428). As there was not any observed effect on molar conversion of LFP by varying flow rates between 30 and 66 mL hr⁻¹, slower flow rates were not investigated. At the other extreme, flow rates of 72 mL hr -1 sometimes resulted in leaks at fixtures/connections, and thus experiments did not exceed 66 mL

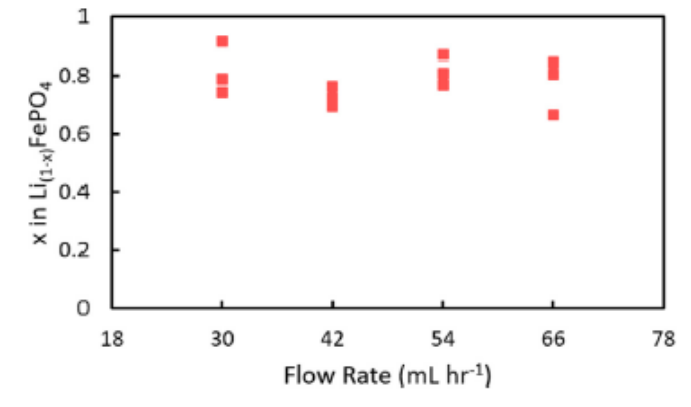


Fig. 6. Conversion of LFP to FP after flowing 60 mL of 0.2 mol L^{-1} [Fe(CN)₈]³⁻ in a 1.0 cm packed bed of LFP at different flow rates, Experimental conditions were run in triplicate and each data point is a different experimental run.

hr⁻¹. Varying flow-rates would affect the bulk transport of the [Fe(CN)₆]³⁻ reactant in the packed bed, and increased conversion with increasing flow rate would have indicated overcoming external mass transport resistances in the PBR (Rawlings and Ekerdt, 2002). The lack of flow rate dependence indicated the PBR was operating in a regime without external mass transport resistances at the secondary LFP/FP particle aggregate surfaces.

3.3.3. Redox shuttle concentration variation

At a bed height of 1.0 cm (with 1.0 g LFP) and a constant flow rate of 54 mL h⁻¹, three concentrations of [Fe(CN)₆]³⁻ solution were evaluated at room temperature: 0.1, 0.2, and 0.3 mol L⁻¹. For each concentration, 60 mL of redox shuttle solution traversed the PBR, meaning the total number of moles ($\times 10^{-3}$) of $[Fe(CN)_6]^{3-}$ through the reactor was 6, 12, and 18 for 0.1, 0.2, and 0.3 mol L-1 concentration, respectively. Thus, the ratio between moles of LFP in packed bed reactor to total moles of $[Fe(CN)_{5}]^{3-}$ fed was 1:1, 1:2, and 1:3 for 0.1, 0.2, and 0.3 mol L⁻¹ concentration, respectively. As shown in Fig. 7a, concentration of redox shuttle impacted the molar conversion of LFP in the packed bed reactor, with faster conversion of the LFP to FP with increasing concentration. The LFP in the PBR was completely delithiated after 60 mL of 0.3 mol L-1 [Fe(CN)6]3- solution passed through, whereas for 0.1 mol L-1 the same volume resulted in ~ 56% conversion of LFP to FP. Due to the different concentrations but same flow rate and total volume, the total stoichiometry of [Fe(CN)6]3-:LFP was different. For 0.3 mol L^{-1} $[Fe(CN)_6]^{3-}$ the total moles fed stoichiometric ratio was 3:1, while for 0.1 mol L^{-1} it was1:1.

Due to the differences in concentration and total moles fed, the conversion of LFP based on total moles of $[Fe(CN)_6]^{3-}$ flowed through the PBR was considered (Fig. 7b). Due to normalizing based on total stoichiometry, the differences in the rate of conversion of LFP were less apparent on the moles of $[Fe(CN)_6]^{3-}$ fed basis. At the end of the 0.1 mol L⁻¹ case $(6 \times 10^{-3} \text{ mol of } [Fe(CN_6)]^{3-}$ flowed through the PBR), the conversion of LFP in for

0.1, 0.2, and 0.3 mol L^{-1} [Fe(CN₆)]³ was 56, 59, and 66 %, respectively. While the magnitude of the differences in LFP conversion on the total moles of reactant fed basis was less than on a volume of reactant solution fed, the difference for the three different concentrations was still significant on the moles reactant fed bases (p = 0.039).

For the experiments with variation of redox concentration, analysis was also conducted on the conversion of LFP with time (Fig. 7c). Due to constant flow rate and feed concentration, the analysis conducted on the basis of effluent volume would be the same. Also, the effluent concentration of the redox shuttle in the oxidized form (e.g., unreacted) as a function of the effluent volume is shown (Fig. 7d), where a horizontal line designates the feed (or equivalently maximum) concentration. As can be seen in these results, although the highest feed concentrations resulted in the greatest oxidation of the LFP, the amount of LFP reacted decreased with time/redox shuttle solution volume faster as the redox shuttle feed concentration was increased. To an extent this would be expected – if the LFP was completely converted rapidly the unreacted redox shuttle in the outlet would reach 100% of the feed concentration upon complete conversion of the solid.

3.3.4. Temperature variation

The effect of varying temperature on the conversion of the PBR with LFP was evaluated at 4.0, 13.0, 22.4, and 40.0 °C. For these experiments, the bed height was kept constant at 1.0 cm bed height, the flow rate was 54 mL h^{-1} , and the $[\text{Fe}(\text{CN})_6]^{3-}$ feed concentration was 0.2 mol L⁻¹. The 22.4 °C temperature was achieved by running the reactor at room temperature in the setup shown in Fig. 1b. For 4, 13, and 40 °C, a water bath was used to keep the PBR at constant temperature. The $[\text{Fe}(\text{CN})_6]^{3-}$ feed solution was also kept at the temperature of the PBR for each temperature.

As shown in Fig. 8, the conversion of LFP in PBR after 60 mL of the feed solution had exited the reactor for 4.0 and 13.0 °C was 53.5% and 75%, respectively, and at 22.4 and 40.0 °C both were

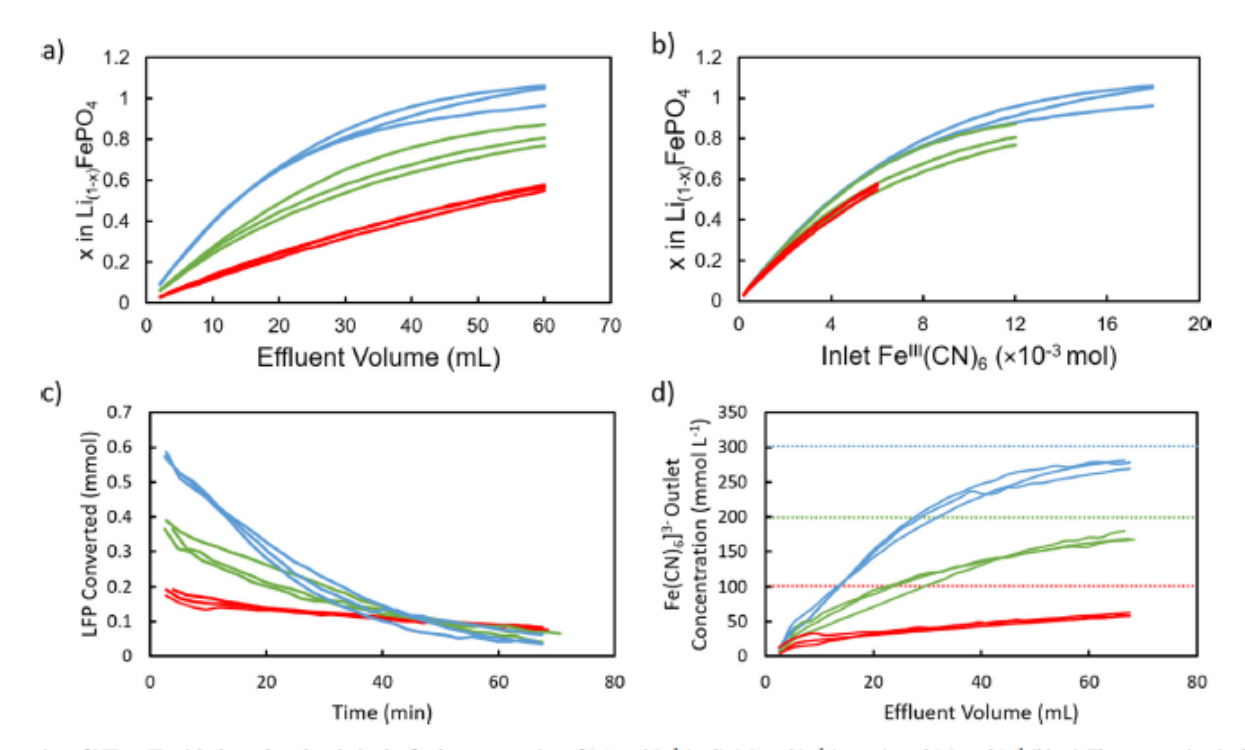


Fig. 7. Conversion of LFP to FP with the redox shuttle in the feed concentration of 0.1 mol L^{-1} (red.), 0.2 mol L^{-1} (green), and 0.3 mol L^{-1} (blue). The conversion is shown on the basis of a) volume of feed solution passed through the reactor and b) total moles of $[\text{Fe}(\text{CN})_6]^3$ -flowed through the reactor, c) Moles of LFP converted in the PBR as a function of time, and d) outlet $[\text{Fe}(\text{CN})_6]^3$ - concentration as a function of effluent volume. The horizontal bars in d) correspond to the initial concentration fed to the PBR. The bed height was 1.0 cm and the flow rate was 54 mL h⁻¹. Experimental conditions were run in triplicate, and each experiment is a different line.

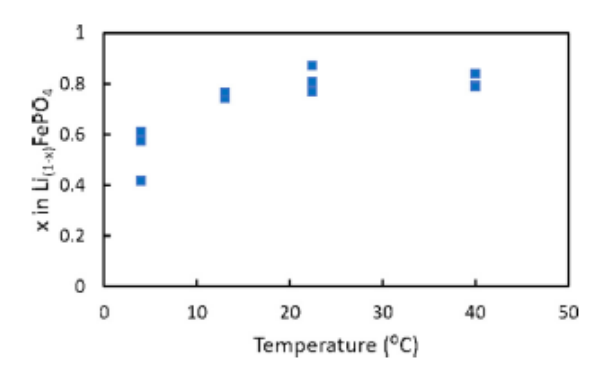


Fig. 8. Conversion of LFP to FP after flowing 60 mL of 0.2 M [Fe(CN)₆]³⁻ through the reactor at different temperatures for 1.0 cm bed-height at 54 mL h⁻¹ solution feed. Triplicates at each temperature are shown in this plot.

similar at ~80%. There was a significant difference between the conversion obtained for the four temperature variations (p = 1.2 × 10⁻³). However, the conversion at 4 °C (53.5%) was much lower than the conversion at higher temperatures. It has been shown previously that phase boundary movement during electrochemical redox in micron sized LFP is controlled by surface reaction (i.e. Li* diffusion in different crystallographic planes) (Huang et al., 2013) and bulk diffusion limitations (solid-state Li* diffusion along [101] direction) (Hong et al., 2017; Srinivasan and Newman, 2006; Oyama et al., 2012). Although these observations were for electrochemical redox in LFP, Li* transport through [101] channels in the crystal plane is a behavior inherent to olivine LFP. Hence, the internal Li* transport behavior was likely similar during chemical redox of LFP. The rate-limiting step in electrochemical investigations has been Li* diffusion-controlled phase boundary movement in the direction perpendicular to the surface, i.e. core-shell mechanism on an individual primary particle level. In a previous temperature dependent electrochemical analysis, the first-order rate constant for delithiation in LiMn_{0.4}Fe_{0.6}PO₄ was shown to decrease by an order of magnitude for a temperature decrease from 20 °C to 0 °C (Xiang et al., 2018). The particle size in that report was 50 nm, similar to this report. It is possible that processes at the primary particle level (electron transfer kinetics and/or solid-state Li* diffusion) become limiting below a threshold temperature for the PBR in this study (at temperatures below 20 °C). [Fe(CN)6]3- transport in the liquid phase would also be slowed at lower temperatures due to the diffusion coefficient dependence of [Fe(CN)₆]³⁻, however, if that was the limiting process across all the temperatures evaluated a difference in conversion would also be expected between the two highest temperatures, and this was not the case.

3.4. Reaction process

The reaction between the redox shuttle, $[Fe(CN)_6]^{3-}$ and LFP in the PBR is an example of a heterogeneous reaction proposed to occur in the following steps:

- External transport of [Fe(CN)₆]³⁻ from the flowing bulk solution in the PBR to the surface of the porous LFP aggregate particles.
- Internal diffusion of [Fe(CN)₆]³⁻ in the fluid-filled porous channels of the LFP aggregates.
- Reaction between LFP and [Fe(CN)₆]³⁻ as described in equation (1) would occur in multiple steps-
- 3a) Adsorption of $[Fe(CN)_6]^{3-}$ on the surface of LFP primary particle.
- 3b) Internal coupled solid-state Li*/e⁻ diffusion to the surface of the primary particles or more locally crystal grains.
- 3c) Electron transfer between $[Fe(CN)_6]^{3-}$ and LFP (with the electron coming from the Fe in the LFP):

$$[Fe(CN)_6]^{3-} + e^- \rightarrow [Fe(CN)_6]^{4-}$$
 (2)

$$LiFePO_4 \rightarrow Li^+ + FePO_4 + e^-$$
 (3)

3d) Desorption of [Fe(CN)₆]⁴⁻ from the surface of LFP.

3e) Transfer of Li* from the solid particle phase to the solution phase.

- 4) Diffusion of the [Fe(CN)₆]⁴⁻ and Li* away from the LFP surface and through the LFP aggregate to the edge of the aggregate secondary particle.
- Transport of the [Fe(CN)₆]⁴ (and Li*) to the bulk fluid passing through the PBR.

According to the proposed reaction steps and experimental observations, it was speculated that the heterogeneous reaction in the PBR follows a shrinking core process with regards to the LFP aggregate particles. Note that this shrinking core description for the LFP aggregates in the PBR is at a much larger length scale (tens of micrometers to millimeters), which is different from LFP phase transitions models which have included shrinking cores that has been discussed for primary particles undergoing electrochemical reactions in LFP electrodes (Malik et al., 2013). For the shrinking core in the PBR, the LFP primary particles on the outer region of the aggregate would convert to FP first, and the conversion of primary LFP particles to FP would then proceed towards the aggregate core. Thus, the diffusion distance of [Fe(CN)₆]³⁻ becomes greater through the pore microstructure and past reacted FP primary particles towards the core to find LFP for undergoing reaction as the reaction time and volume of feed solution progressed. The independence of conversion with flow rate suggested external mass transport resistance to the [Fe(CN)₆]³⁻ entering the LFP particle aggregates was not influencing the LFP conversion. For the bed height variation experiments, as the bed was made taller the [Fe (CN)₆|3- concentration in the outlet remained lower for longer (and thus conversion of LFP in the packed bed was higher for longer). This outcome would be consistent with the [Fe(CN)₆]³ reacting with the more easily accessible outer regions of the LFP particles first, and then as [Fe(CN)6]3- must diffuse further in the LFP aggregates to react the conversion of [Fe(CN)₆]³⁻ tapers off. For the longer column that tapering off would be delayed due to more total LFP particle aggregates available and thus more total moles of LFP that were less limited by transport of the soluble redox shuttle through the microstructure. For the experiments where $[Fe(CN)_6]^{3-}$ concentration was varied, not only did the highest concentration have the highest conversion on a volume of feed solution basis (Fig. 7a), but also on a total moles fed basis (Fig. 7b). For the moles fed basis, this may have been because the higher concentration redox shuttle solution can achieve higher concentrations deeper into the pellet, which would increase the overall moles reacted. With regards to temperature, molar conversion of LFP was found to decrease significantly at 4.0 and 13.0 °C, but was unaffected at 22.4 and 40 °C. The temperature insensitivity at the highest temperatures would be consistent with the shrinking core concept, as the expected change in the diffusion coefficient of the [Fe(CN)₆]³⁻ in the liquid would be relatively small (<10%). However, the transition to much lower conversion at the lowest temperatures suggests a new process may be playing a role. For LFP, previous electrochemical measurements have suggested the oxidation kinetics for LFP undergo a dramatic decrease at 20 °C (Xiang et al., 2018), suggesting that after a certain temperature that the kinetics rather than the transport may become the rate limiting process. Understanding and confirming the rate limiting process for the PBR under different conditions will continue to be the focus of future efforts and characterization development.

It is noted here that LFP has been well known as a fast charge/discharge (oxidation/reduction) material in electrochemical studies (Tang et al., 2011; Huang et al., 2013). However, the electrodes are typically less than 200 µm thick. For this study, most of the capacity came from particles in aggregates which were a couple

of mm from the core to the surface. For such thick porous aggregate sizes, the analogy to limitation in an electrochemical system would be for much thicker electrodes where solution-phase transport limitations limit the rate of the electrochemical reactions. Such phenomena has been reported, for example porous thick sintered electrodes (from few hundred μm to couple mm thickness) have been characterized where the interstitial Li* transport in the electrolyte phase through tortuous paths has been responsible for limiting electrochemical reaction rates (Robinson et al., 2018), and thus high rates of discharge were not accessible due to electrolyte depletion (Nie et al., 2020). For the PBR reactor, the description of the limiting process postulated above is similar in that it is transport of a species through the electrolyte phase in the interstitial regions between particles, although the species in the PBR was the redox shuttle rather than Li*.

The PBR reactor system was similar to that of chemical looping combustion, where gaseous fuel/ air reacts with metal oxide particles (Lyngfelt, 2020). Metal oxides are reduced and oxidized in a fuel reactor and air reactor, respectively, and are transferred to separate reactors for oxidation and reduction. Despite this operational/application difference (and relevant contacting phases in many cases), it is like the PBR system in that the particles forming the packed bed are themselves reactants that have spatial and temporal functionalities sensitive to the reaction progression. Therefore, qualitative inferences could be derived from the chemical looping combustion. For instance, a comparison done on pilotscale fuel reactors of 1 MW, 100 kW, and 50 kW capacity found that intermediate sizes (90-300 µm) of metal oxide particles (i.e. the solid reactant) were preferred (Lyngfelt, 2020). If the particles were too big (>8 mm), there was insufficient conversion. If the particles were too small, they were elutriated into the gas stream. Additionally, the ideal particle size distributions vary between pilot scale and full-scale plants (100-1000 MW), as the residence time for gases was higher in full-scale plants. The impact of aggregate size distributions on the PBR system will be explored in future work, as the processes used to make the aggregates in this study did not lend to control over aggregate size. Analogous to chemical looping combustion, in the chemical reservoir of a RTFB, it will be desirable to convert the fluid reactant stream 100% with every flow cycle. Hence, particle engineering of solid electroactive material is expected to impact the molar conversion of redox shuttles for RTFBs and other redox shuttle/electroactive material coupled chemical redox applications.

4. Conclusion

In this work, a reactor system was reported which enabled evaluation of the extent of chemical oxidation of a solid Li-ion electroactive material, LFP, with a dissolved redox shuttle compound. The conversion in the reactor was tracked as a function of time for variations of different reactor conditions: bed-height, concentration of redox shuttle, flow rate of feed solution, and operating temperature. The dependence between molar conversion of LFP and the different variables was assessed using single variable ANOVA. It was found that flow rate did not influence the conversion, and bed-height did not impact the molar conversion of LFP when stoichiometric amounts of shuttle were flowed. It was also found that the molar conversion of LFP has a strong dependence on the concentration of the redox shuttle. Additionally, it was observed that at the highest temperatures that there was not a temperature dependence, but that below a certain operating temperature the molar LFP conversion became dependent upon temperature. A reaction mechanism based on these observations was suggested where a shrinking core of LFP conversion to FP propagated at the LFP aggregate level, where for most reaction conditions the conversion was limited by the process of the redox shuttle diffusion in the solution phase though the LFP aggregate microstructure. This study provides a framework for investigating packed beds of Li-ion electroactive materials undergoing chemical redox, which is relevant for redox targeting flow battery applications and potentially others such as the recycling and extraction of Li* from spent Li-ion battery materials.

CRediT authorship contribution statement

Devanshi Gupta: Conceptualization, Validation, Formal analysis, Investigation, Writing – original draft, Writing – review & editing, Visualization. Yuxuan Zhang: Investigation, Visualization. Ziyang Nie: Investigation. Jing Wang: Validation, Investigation, Visualization. Gary M. Koenig: Conceptualization, Resources, Writing – review & editing, Supervision, Funding acquisition.

Declaration of Competing Interest

The authors declare that they have no known competing financial interests or personal relationships that could have appeared to influence the work reported in this paper.

Acknowledgement

This project was funded by the National Science, through awards IIP-1940915 and CBET-1652488. This research used resources at the High Flux Isotope Reactor, a DOE Office of Science User Facility operated by the Oak Ridge National Laboratory under contract with UT-Battelle, LLC.

This manuscript has been in part authored by UT-Battelle, LLC under Contract No. DE-AC05-000R22725 with the U.S. Department of Energy. The United States Government retains and the publisher, by accepting the article for publication, acknowledges that the United States Government retains a non-exclusive, paid-up, irrevocable, world-wide license to publish or reproduce the published form of this manuscript, or allow others to do so, for United States Government purposes. The Department of Energy will provide public access to these results of federally sponsored research in accordance with the DOE Public Access Plan (http://energy.gov/downloads/doe-public-access-plan).

Appendix A. Supplementary material

Supplementary data to this article can be found online at https://doi.org/10.1016/j.ces.2022.117443.

References

Gür, T.M., 2018. Review of electrical energy storage technologies, materials and systems; challenges and prospects for large-scale grid storage. Energy Environ. Sci. 11, 2696–2767. https://doi.org/10.1039/c8ee01419a.

Dunn, B., Kamath, H., Tarascon, J.-M., 2011. Electrical energy storage for the grid: a battery of choices. Science 334 (6058), 928–935.

Wang, W., Luo, Q., Li, B., Wei, X., Li, L., Yang, Z., 2013. Rec. Progr. Redox Flow Batt. Res. Dev., 970–986 https://doi.org/10.1002/adfm.201200694.

Yan, R., Wang, Q., 2018. Redox-targeting-based flow batteries for large-scale energy storage. Adv. Mater. 1802406, 1802406. https://doi.org/10.1002/ adma.201802406.

Vivo-Vilches, J.F., Nadeina, A., Rahbani, N., Seznec, V., Larcher, D., Baudrin, E., 2021. LiFePO₄-ferri/ferrocyanide redox targeting aqueous posolyte: Set-up, efficiency and kinetics. J. Power Sources. 488, 229387. https://doi.org/10.1016/j. jpowsour.2020.229387.

Páez, T., Martínez-Cuezva, A., Palma, J., Ventosa, E., 2019. Mediated alkaline flow batteries: From fundamentals to application. ACS Appl. Energy Mater. 2 (11), 8328–8336. https://doi.org/10.1021/acsaem.9b0182610.1021/ acsaem.9b01826.s001.

Wong, C.M., Sevov, C.S., 2021. All-organic storage solids and redox shuttles for redox-targeting flow batteries. ACS Energy Lett., 1271–1279 https://doi.org/ 10.1021/acsenergylett.1c00143.

- Zanzola, E., Dennison, C.R., Battistel, A., Peljo, P., Vrubel, H., Amstutz, V., Girault, H. H., 2017. Redox solid energy boosters for flow batteries: polyaniline as a case study. Electrochim. Acta. 235, 664–671. https://doi.org/10.1016/ j.electacta.2017.03.084.
- Jia, C., Pan, F., Zhu, Y.G., Huang, Q., Lu, L., Wang, Q., 2015. High energy density nonaqueous all redox flow lithium battery enabled with a polymeric membrane, Sci. Adv. 1, 1–7. https://doi.org/10.1126/sciadv.1500886.
- Duduta, M., Ho, B., Wood, V.C., Limthongkul, P., Brunini, V.E., Carter, W.C., Chiang, Y.-M., 2011. Semi-solid lithium rechargeable flow battery. Adv. Energy Mater. 1 (4), 511–516. https://doi.org/10.1002/aenm.201100152.
- Qi, Z., Koenig, G.M., 2017. Review article: flow battery systems with solid electroactive materials. J. Vac. Sci. Technol. B, Nanotechnol. Microelectron. Mater. Process. Meas. Phenom. 35, https://doi.org/10.1116/ 1.4983210 040801.
- Chalamala, B.R., Soundappan, T., Fisher, G.R., Anstey, M.R., Viswanathan, V.V., Perry, M.L., 2014. Redox flow batteries: an engineering perspective. Proc. IEEE. 102, 976–999. https://doi.org/10.1109/JPROC.2014.2320317.
- Huang, Q., Li, H., Grätzel, M., Wang, Q., 2013. Reversible chemical delithiation/ lithiation of LiFePO₄: towards a redox flow lithium-ion battery. Phys. Chem. Chem. Phys. 15, 1793–1797. https://doi.org/10.1039/c2cp44466f.
- Gupta, D., Koenig, G.M., 2020. Analysis of chemical and electrochemical lithiation/ delithiation of a lithium-ion cathode material. J. Electrochem. Soc. 167., https:// doi.org/10.1149/1945-7111/ab6bbf 020537.
- Gupta, D., Cai, C., Koenig, G.M., 2021. Comparative analysis of chemical redox between redox shuttles and a lithium-ion cathode material via electrochemical analysis of redox shuttle conversion. J. Electrochem. Soc. 168, https://doi.org/ 10.1149/1945-7111/ac0068 050546.
- Pan, F., Yang, J., Huang, Q., Wang, X., Huang, H., Wang, Q., 2014. Redox targeting of anatase TiO₂ for redox flow lithium-ion batteries. Adv. Energy Mater., n/a-n/a https://doi.org/10.1002/aenm.201400567.
- Yan, R., Ghilane, J., Phuah, K.C., Pham Truong, T.N., Adams, S., Randriamahazaka, H., Wang, Q., 2018. Determining Li *-coupled redox targeting reaction kinetics of battery materials with scanning electrochemical microscopy. J. Phys. Chem. Lett., 491–496 https://doi.org/10.1021/acs.jpclett.7b03136.
- Cussler, E.L., Cussler, E.L., 2009. Diffusion: mass transfer in fluid systems. Cambridge University Press.
- Chung, S.-Y., Bloking, J.T., Chiang, Y.-M., 2002. Electronically conductive phosphoolivines as lithium storage electrodes. Nat. Mater. 1 (2), 123–128. https://doi. org/10.1038/nmat732.
- Yu, J., Wang, X., Zhou, M., Wang, Q., 2019. A redox targeting-based material recycling strategy for spent lithium ion batteries. Energy Environ. Sci. 12 (9), 2672–2677.
- Li, Q.i., Li, N.a., Ishida, M., Zhou, H., 2015. Saving electric energy by integrating a photoelectrode into a Li-ion battery. J. Mater. Chem. A 3 (42), 20903–20907.
- Liao, S., Zong, X., Seger, B., Pedersen, T., Yao, T., Ding, C., Shi, J., Chen, J., Li, C., 2016. Integrating a dual-silicon photoelectrochemical cell into a redox flow battery for unassisted photocharging. Nat. Commun. 7. https://doi.org/10.1038/ ncomms11474.
- Zhang, L., Zhang, Z., Amine, K., 2012. Redox shuttle additives for lithium-ion battery. Lithium Ion Batter. - New Dev. https://doi.org/10.5772/26572.
- Moshurchak, L.M., Buhrmester, C., Dahn, J.R., Wei, X., Xu, W., Huang, J., Zhang, L., Walter, E., Lawrence, C., Vijayakumar, M., Henderson, W.A., Liu, T., Cosimbescu, L., Li, B., Sprenkle, V., Wang, W., Rogers, E.I., Silvester, D.S., Poole, D.L., Aldous, L., Hardacre, C., Compton, R.G., 2005. Spectroelectrochemical studies of redox shuttle overcharge additive for LifePO₄-based Li-ion batteries. J. Electrochem. Soc. 112, 2729–2735. https://doi.org/10.1149/1.1896327.
- Baur, J.E., Wightman, R.M., 1991. Diffusion coefficients determined with microelectrodes. J. Electroanal. Chem. 305 (1), 73–81. https://doi.org/10.1016/ 0022-0728(91)85203-2.
- Padhi, A.K., Nanjundaswamy, K.S., Goodenough, J.B., 1997. Phospho-olivines as positive-electrode materials for rechargeable lithium batteries. J. Electrochem. Soc. https://doi.org/10.1149/1.1837571.
- Yuan, L.-X., Wang, Z.-H., Zhang, W.-X., Hu, X.-L., Chen, J.-T., Huang, Y.-H., Goodenough, J.B., 2011. Development and challenges of LiFePO 4 cathode material for lithium-ion batteries. Energy Environ. Sci. 4 (2), 269–284. https:// doi.org/10.1039/COEE00029A

- Luo, J., Sam, A., Hu, B., DeBruler, C., Wei, X., Wang, W., Liu, T.L., 2017. Unraveling pH dependent cycling stability of ferricyanide/ferrocyanide in redox flow batteries. Nano Energy 42, 215–221. https://doi.org/10.1016/j.nanoen.2017.10.057.
- Lepage, D., Sobh, F., Kuss, C., Liang, G., Schougaard, S.B., 2014. Delithiation kinetics study of carbon coated and carbon free LiFePO₄. J. Power Sources. 256, 61–65. https://doi.org/10.1016/j.jpowsour.2013.12.054.
- Zubi, G., Dufo-López, R., Carvalho, M., Pasaoglu, G., 2018. The lithium-ion battery: State of the art and future perspectives. Renew. Sustain. Energy Rev. 89, 292–308. https://doi.org/10.1016/j.rser.2018.03.002.
- Gong, K., Fang, Q., Gu, S., Li, S.F.Y., Yan, Y., 2015. Nonaqueous redox-flow batteries: organic solvents, supporting electrolytes, and redox pairs. Energy Environ. Sci. 8, 3515–3530. https://doi.org/10.1039/C5EE02341F.
- Luo, J., Hu, B.o., Debruler, C., Bi, Y., Zhao, Y.u., Yuan, B., Hu, M., Wu, W., Liu, T.L., 2019.
 Unprecedented capacity and stability of ammonium ferrocyanide catholyte in ph neutral aqueous redox flow batteries. Joule. 3 (1), 149–163. https://doi.org/10.1016/j.joule.2018.10.010.
- Chen, Y., Zhou, M., Xia, Y., Wang, X., Liu, Y., Yao, Y., Zhang, H., Li, Y., Lu, S., Qin, W., Wu, X., Wang, Q., 2019. A stable and high-capacity redox targeting-based electrolyte for aqueous flow batteries. Joule. 3 (9), 2255–2267. https://doi.org/10.1016/j.joule.2019.06.007.
- Gaberscek, M., Dominko, R., Jamnik, J., 2007. Is small particle size more important than carbon coating? An example study on LiFePO₄ cathodes. Electrochem. Commun. 9 (12), 2778–2783. https://doi.org/10.1016/j.elecom.2007.09.020.
- Ravet, N., Gauthier, M., Zaghib, K., Goodenough, J.B., Mauger, A., Gendron, F., Julien, C.M., 2007. Mechanism of the Fe³⁺ reduction at low temperature for LiFePO₄ synthesis from a polymeric additive. Chem. Mater. 19, 2595–2602. https://doi.org/10.1021/cm070485r.
- W.C. Navidi, Statistics for engineers and scientists, McGraw-Hill Higher Education New York, NY, USA, 2008.
- Rawlings, J.B., Ekerdt, J.G., 2002. Chemical reactor analysis and design fundamentals. Nob Hill Pub Llc.
- Malik, R., Abdellahi, A., Ceder, G., 2013. A critical review of the Li insertion mechanisms in LiFePO₄ electrodes. J. Electrochem. Soc. 160 (5), A3179–A3197. https://doi.org/10.1149/2.029305jes.
- Hong, L., Li, L., Chen-Wiegart, Y.K., Wang, J., Xiang, K., Gan, L., Li, W., Meng, F., Wang, F., Wang, J., Chiang, Y.M., Jin, S., Tang, M., 2017. Two-dimensional lithium diffusion behavior and probable hybrid phase transformation kinetics in olivine lithium iron phosphate. Nat. Commun. 8. https://doi.org/10.1038/s41467-017-01315-8.
- Srinivasan, V., Newman, J., 2006. Existence of path-dependence in the LiFePO₄ electrode. Electrochem. Solid-State Lett. 9, A110. https://doi.org/10.1149/1.2159299.
- Oyama, G., Yamada, Y., Natsui, R.-I., Nishimura, S.-I., Yamada, A., 2012. Kinetics of nucleation and growth in two-phase electrochemical reaction of Li xFePO₄. J. Phys. Chem. C. 116 (13), 7306–7311. https://doi.org/10.1021/jp300085n.
- Xiang, K., Yang, K., Carter, W.C., Tang, M., Chiang, Y.M., 2018. Mesoscopic phase transition kinetics in secondary particles of electrode-active materials in lithium-ion batteries. Chem. Mater. https://doi.org/10.1021/acs. chemmater.7b05407.
- Tang, K., Yu, X., Sun, J., Li, H., Huang, X., 2011. Kinetic analysis on LiFePO₄ thin films by CV, GITT, and EIS. Electrochim. Acta. 56 (13), 4869–4875. https://doi.org/ 10.1016/j.electacta.2011.02.119.
- Huang, S.J., Huang, B.G., Pai, F.S., 2013. Fast charge strategy based on the characterization and evaluation of LiFePO₄ batteries. IEEE Trans. Power Electron. 28, 1555–1562. https://doi.org/10.1109/TPEL.2012.2209184.
- Robinson, J.P., Ruppert, J.J., Dong, H., Koenig, G.M., 2018. Sintered electrode full cells for high energy density lithium-ion batteries. J. Appl. Electrochem. 48 (11), 1297–1304. https://doi.org/10.1007/s10800-018-1242-y.
- Nie, Z., Ong, S., Hussey, D.S., LaManna, J.M., Jacobson, D.L., Koenig, G.M., 2020. Probing transport limitations in thick sintered battery electrodes with neutron imaging. Mol. Syst. Des. Eng. 5 (1), 245–256.
- Lyngfelt, A., 2020. Chemical looping combustion: status and development challenges. Energy Fuels 34 (8), 9077–9093. https://doi.org/10.1021/acs. energyfuels.0c01454.
- Kuss, C., Carmant-Dérival, M., Trinh, N.D., Liang, G., Schougaard, S.B., 2014. Kinetics of heterosite iron phosphate lithiation by chemical reduction. J. Phys. Chem. C. 118 (34), 19524–19528. https://doi.org/10.1021/jp502346f.